Probing molecular layers with low-energy electrons

Tebyani, A.

2

Low Energy Electron Microscopy

Abstract

In this chapter, we introduce Low Energy Electron Microscopy (LEEM). We will describe the operation of LEEM and explain the various measurement techniques available in LEEM that are used in the following chapters.

2.1 Introduction

Low Energy Electron Microscopy (LEEM) was first realized in 1985 by Wolfgang Telieps and Ernst Bauer. [1] Because of the low energy of incident electrons when they interact with the sample, typically only a few electron volts, LEEM is particularly suitable for probing the surface of the sample. This is a consequence of the small mean free path of electrons at such low energies, about one to a few nanometers. [2,3] Combined with the advantage of simultaneous illumination of the entire field of view, as opposed to scanning probe techniques such as Scanning Tunneling Microscopy (STM), LEEM has been successfully employed to study a variety of dynamic phenomena at surfaces in real time. Prominent examples include phase transitions, and growth of molecular crystals, oxide films, metals, two-dimensional materials, etc. [4–19] The ability to follow changes in the sample in real time is particularly powerful noting that it holds true for any of the various techniques for imaging and spectroscopy available in LEEM. Several of these measurement techniques are explained in this chapter.

The LEEM instrument used for the measurements in this dissertation is the ESCHER LEEM instrument at Leiden University. [20] Here, ESCHER stands for **E**lectronic, **S**tructural and **CHE**mical nanoimaging in **R**eal-time. The ESCHER LEEM instrument is based on an aberration-corrected version [21,22] of the IBM/SPECS LEEM instrument designed by Rudolf Tromp and first introduced in 1998. [23] Its sample chamber has an UltraHigh Vacuum (UHV) pressure of $\sim 1\times10^{-9}$ mbar or lower, with experiments possible at gas pressures up to 1×10^{-5} mbar. Measurements and sample preparation can be performed at sample temperatures from room temperature up to 1800 K. A Knudsen cell evaporator connected to the sample chamber allows for *in situ* sublimation of various materials such as metals or molecules. A schematic of the LEEM instrument is illustrated in Fig. 2.1. The ESCHER instrument is also equipped with a cryogenic sample chamber, omitted from this schematic. The cryogenic extension of the microscope is discussed in detail in chapter 7.

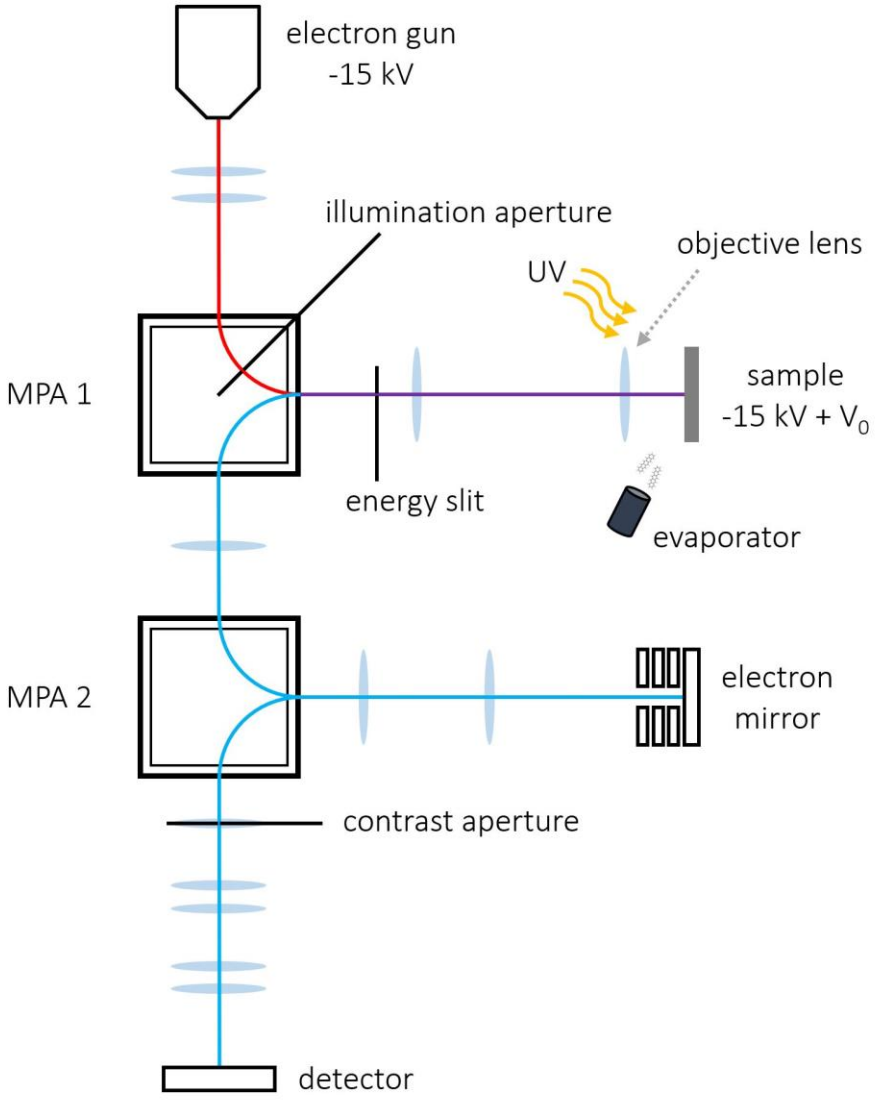

Fig. 2.1 Schematic of LEEM instrument. A beam of electrons is emitted from the electron gun at the top and traverses the column with a kinetic energy of 15 keV along the red line. MPA1 bends the electron beam toward the sample. An electric field between the objective lens and the sample decelerates the electrons to a kinetic energy of eV_0. The electrons interact with the sample with this energy, which is tunable by setting the sample potential. Reflected electrons are accelerated by the same electric field and directed toward MPA1, and follow the blue trajectory toward the detector. The purple line shows where the paths of the incident and reflected electrons overlap. MPA2 works in the same manner as MPA1 but directs the electrons to an electrostatic electron mirror, which corrects the lowest-order aberrations of the microscope. Imaging with photoelectrons is also possible via a Hg UV lamp attached to the sample chamber. Furthermore, a Knudsen cell evaporator connected to the sample chamber allows for *in situ* molecule sublimation. Various lenses and apertures of the microscope are also shown in the figure.

2.2 Imaging in LEEM

LEEM includes a variety of magnetic and electrostatic components, which are employed to focus, disperse, deflect or otherwise adjust the electron beam. Imaging with electrons proceeds in the following way. Electrons are emitted from an electron gun, located at the top in Fig. 2.1. The electron source is a cold-field emitter, in which electrons are extracted from a sharp cathode due to a strong electric field between the cathode and a planar anode inside the gun, via a mechanism called Fowler-Nordheim emission. [24] This manner of electron beam generation leads to a narrower spread in the energy of the electrons, about 250 meV, compared to alternatives such as thermionic emission. After emission from the tip, the electrons are accelerated to a kinetic energy of 15 keV, and traverse the column with this energy. Several magnetic lenses and deflectors in the illumination column, i.e. before magnetic prism array 1 (MPA1), are used to focus and adjust the electron beam, such as vary the beam diameter or beam tilt. MPA1 bends the electron beam by 90˚ toward the objective lens and the sample. The LEEM is a cathode lens instrument, with the sample acting as the cathode. The electrons are decelerated by an electric field of ~10 kV/mm between a grounded objective lens, and the sample, which is biased at -15 kV+V_0 (close to the electron gun potential) and located 1-2 millimeters away from the front of the objective lens. After deceleration, a collimated beam of electrons with a kinetic energy of $eV_0+\Delta\Phi$ reaches and interacts with the sample. Here, $\Delta\Phi$ represents the difference between the work functions of the sample and the electron gun. The interaction energy can be precisely tuned by changing the sample bias potential, with typical values of 0-50 eV. After reflection from the sample, the electrons are re-accelerated by the same electric field between the objective lens and the sample to an energy of ~15 keV. The objective lens forms a magnified real-space image of the sample using a magnetic lens field, and directs the electrons toward MPA1. This time, the Lorentz force exerted by the prism bends the electron beam by 90˚ downwards (see the schematic). Hence, the prism separates the incident and the reflected beams. Magnetic prism array 2 (MPA 2) operates in the same manner as MPA 1, except it directs the electron beam toward an electron mirror. MPA 2 and the electron mirror comprise the aberration-correcting part of the instrument. Aberrations are corrected upon reflection from the mirror. The reflected beam is then bent by MPA 2 toward the detector, travelling through several magnetic lenses (i.e. the projector column) along its path. In the detector, the electrons are first multiplied by a micro-channel plate, and subsequently hit a phosphorescent screen, creating an image that is captured by a CCD camera.

Regarding aberration correction, the electron mirror is comprised of four silicon-bronze discs, one biased at ground potential and the three others at adjustable (negative) high potentials. The ratio of the potentials between the disks determines the optical properties of

the mirror. Aberration correction removes the lowest-order chromatic and spherical aberrations, which are caused predominantly by the cathode objective lens. As a result, the resolution is enhanced from 4.1 nm in the uncorrected version of the instrument, to 1.4 nm after aberration correction. [21] The electron mirror cannot correct higher order or higher rank aberrations, i.e. only C_c and C_3 are corrected. We also note that the LEEM instrument is installed on a vibration isolation foundation, accompanied by an active vibration damping system, in order to reduce mechanical instabilities that can deteriorate the resolution. Furthermore, all the electronic power supplies are highly stable with noise levels of only about 1 ppm, a critical requirement for high-resolution imaging.

In a LEEM instrument, it is also possible to project a reciprocal-space, rather than a real-space, image on the detector screen by changing the excitations of the magnetic lenses in the projector column (i.e. between MPA 2 and the detector). This makes it possible to observe the Low Energy Electron Diffraction (LEED) pattern on the detector screen. The reciprocal-space image contains information about the angular distribution of electrons. We note that since only the out-of-plane momentum of the electrons is affected by the cathode lens electric field, the in-plane momenta of the electrons from the sample are preserved in the LEED image. Given that the wavelengths of the electrons used in LEEM are on the order of a few Ångstroms (5 Å for 6 eV electrons), surface atomic lattices of crystalline samples act as a diffraction grating for the incoming electrons, creating bright spots in the diffraction image at in-plane momenta where the Bragg conditions for constructive interference of scattered electron waves are satisfied. Hence, the diffraction pattern conveys information about the crystalline structure of the sample surface. Combined with real-space information about the surface morphology, the microstructure of the sample can now be characterized.

Diffraction images contain more information than just the position of the diffraction peaks. Study of changes in the profile of the diffraction spots over time or as a result of external stimuli is called Spot Profile Analysis LEED (SPA-LEED). In chapter 4, we use this technique to study electron beam irradiation damage in pentacene films.

In LEEM, real-space and reciprocal-space planes alternatingly follow each other, with the various electron optical elements projecting these planes onto the next element, with possible adjustments in magnification or rotation. Using an analogy with light optics, Fig. 2.2 illustrates the formation of a diffraction image in the back focal plane of an objective lens (plane 1), as well as an inverted real-space image further away (plane 2). In LEEM, due to the effect of the electric field between the objective lens and the sample on the electrons, the trajectories of the rays from the sample are actually parabolic. But the electric field by itself also forms a virtual image of the sample, at a somewhat greater distance to the grounded front

of the objective lens. Taking this virtual image of the sample as the object, Fig. 2.2 applies without modification (i.e. straight-line trajectories).

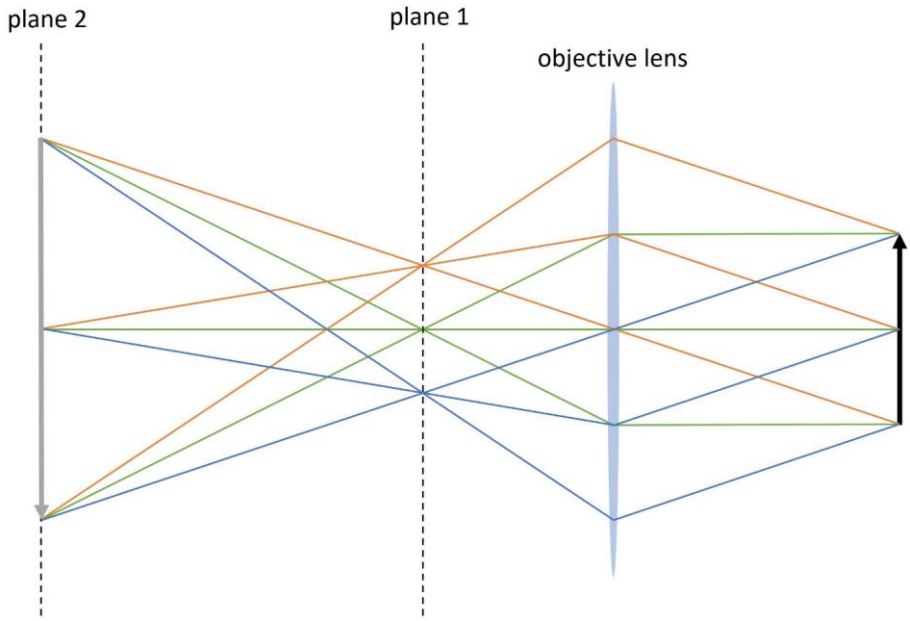

Fig. 2.2 Illustration of image formation in an optical system. The black arrow at the right represents the object. The orange, green and blue lines are optical rays from the object. Planes 1 and 2 indicate diffraction-space and real-space planes after the objective lens, respectively. The grey arrow at the left shows an inverted image of the object. In LEEM, the trajectory of the electrons from the sample is actually parabolic, due to the electric field between the sample and the objective lens.

The ESCHER instrument allows for insertion of apertures along various real-space or diffraction planes. This capability greatly enhances the ability to perform various imaging and spectroscopy techniques, as we describe in the remainder of this chapter. For example, frequently, the area on the sample illuminated by the electron beam is not homogeneous within a beam diameter of several micrometers. To collect information only from smaller homogeneous regions, we can place an aperture along the beam's path in order to limit the illuminated area on the sample surface. Fig. 2.1 shows such an illumination aperture inserted along the diagonal of MPA 1, allowing for selection of sub-micrometer areas on the sample. Placing such an aperture with the goal of investigating the diffraction corresponding to the chosen real-space area is called micro-LEED (μLEED) imaging. Also, with the aperture blocking some of the beam, we can record small fluctuations of the beam current (~pA) which

are not detectable by the electron gun electronics, in order to correct for the noise in the measured data caused by such small fluctuations.

Fig. 2.3 shows an example of LEEM and μLEED imaging, in order to study the microstructure of a pentacene film. Regions with different intensities in Fig. 2.3(a) indicate different layer counts in the pentacene layer, with higher layer counts appearing brighter. In other words, the film thickness is not homogeneous across the illuminated area. Intensity variations between different regions are explained later in this chapter, in the discussion of "LEEM-IV spectroscopy". By placement of an aperture smaller than 1 μm in diameter on regions corresponding to each of the different layer counts, we examined their diffraction patterns. The illuminated areas are indicated with orange, green and blue circles in Fig. 2.3(a), with their associated μLEED patterns in Fig. 2.3(b-d), enclosed with a circle of the same color. The center spot in each image corresponds to specularly reflected electrons, while the other spots are characteristic of the herringbone lattice structure of the pentacene layers. The μLEED images are similar in all three regions, with the diffraction spots appearing increasingly sharper on thicker areas, an indication of better crystallinity. We also note an absence of rotation between the μLEED patterns, signaling that the layers grow on top of each other as a single crystal.

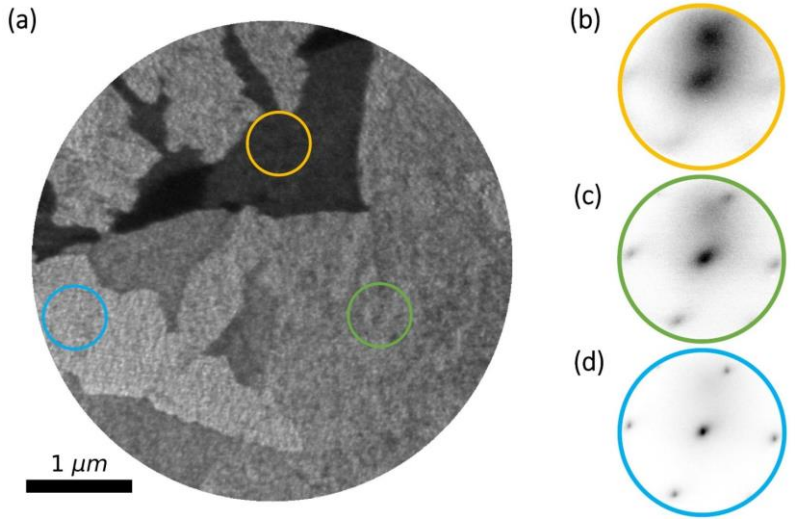

Fig. 2.3 μLEED imaging. (a) Bright-field image of a pentacene film, obtained by a beam of 1.9 eV electrons. Intensity variations within the image indicate non-homogeneity of layer count. The orange, green and blue circles in (a) indicate the locations of the illumination aperture for μLEED imaging. (b-d) diffraction patterns corresponding to the chosen areas in (a), imaged by 11 eV electrons. The colors of the circles around the diffraction patterns correspond to the areas selected by the illumination aperture in (a). The diffraction patterns corresponding to brighter areas (higher layer counts) appear sharper, an indication of better crystallinity. Also, lack of rotation between the diffraction patterns indicates that the layers grow on top of each other as a single crystal.

2.3 Bright-field and dark-field imaging

In the example above, we placed an aperture in a real-space image plane (MPA 1 diagonal) to select certain areas of the sample surface in order to investigate their corresponding diffraction. Similarly, we can place an aperture in a diffraction plane in order to let through only the electrons from a certain diffraction peak, and block the rest. Such an aperture is shown in Fig. 2.1, named "contrast aperture". In the resulting real-space image after such filtering, only areas on the sample surface that contribute to the chosen diffraction peak lighten up. If the aperture lets through only the 0^{th}-order diffraction spot, i.e. normal incidence and reflection of electrons, the resulting real-space image is called a "bright-field" image. The intensities in a bright-field image contain information about the unoccupied electronic density of states (DOS) of the material, as will be explained in the discussion of "LEEM-IV spectroscopy". If any other diffraction spot is selected, the resulting image is called a "dark-field" image. Dark-field imaging differentiates between regions of the image that have different crystal structure or orientations. In chapter 3, we employ bright-field and dark-field imaging to investigate a crystalline pentacene layer on graphite (Fig. 3.3 in chapter 3).

2.4 Photoemission

So far, we have discussed imaging using electrons from the electron gun. The LEEM instrument is also equipped with two ultraviolet (UV) light sources, namely a Hg discharge lamp ($h\nu = 4.9$ eV) and a Helium I/II light source ($h\nu = 21.2$ eV and 40.8 eV). These sources allow for the possibility of imaging with photoelectrons emitted from the sample, or PhotoElectron Emission Microscopy (PEEM). The photoelectrons are accelerated to a kinetic energy of ~15 keV by the same electric field between the objective lens and the sample, and afterwards follow the same path as the reflected electrons from the electron gun. Given that the photons from the Hg lamp illuminate the entire sample surface at once, PEEM can be used to monitor surface phenomena at a larger field of view of several tens of μm. We use PEEM with a Hg lamp to study the dynamics of growth of pentacene layers on various substrates, as will be discussed in chapters 3 and 5.

PEEM and other photoemission imaging and spectroscopy techniques, such as Angle-Resolved PhotoEmission Spectroscopy (ARPES), are widely used in condensed matter physics and surface science to probe the occupied electronic bands in solids. Simply put, if the energy of the incoming photons is higher than the ionization energy of the sample (i.e. the minimum amount of energy required to extract a photoelectron from the sample), photoelectrons can generally be ejected from occupied states in the material. In chapter 5, we

additionally study the role of unoccupied electronic states above the vacuum level, measurable by LEEM-IV spectroscopy (see below), in photoemission.

2.5 Sample preparation

Now, we briefly discuss sample preparation inside the LEEM instrument. As mentioned earlier, a Knudsen cell evaporator can be attached to the sample chamber, allowing for molecule sublimation by resistive heating of the crucible inside the evaporator. The sublimated molecules follow a line of sight from the crucible to the sample surface in the UHV pressure of the sample chamber. Upon reaching the sample surface, they may be adsorbed on the surface via van der Waals forces (physisorption) or formation of chemical bonds with the surface (chemisorption), depending on the substrate. The substrate temperature also plays an important role in adsorption and layer formation. At higher temperatures the incoming molecules (or atoms) can diffuse more easily on the surface, an important factor in the formation of crystalline layers. On the other hand, temperatures that are too high may prevent the incoming molecules from staying on the surface. In this dissertation, we explore the growth of crystalline pentacene layers on a variety of substrates, such as silicon, silicon oxide, as well as van der Waals substrates graphite and hexagonal boron-nitride (hBN). The results are presented in chapters 3 and 5.

Prior to thin film growth, the substrate is prepared *in situ*. An electron bombardment heater behind the sample can heat the sample up to ~1500˚C. This heater was frequently used to prepare atomically-flat silicon surfaces by removing the SiO_2 layer at high temperatures (~1100˚C). For some experiments, the substrates were prepared outside the vacuum system and then transferred into the LEEM instrument. Examples of such substrates include hBN and graphite flakes exfoliated onto SiO_2 surfaces using Scotch tape. [25,26] For these substrates, the heater was used to clean the flake surfaces from adsorbates by keeping the samples at elevated temperatures, such as 500˚C, for several hours. All the substrates were cooled to (near) room temperature prior to pentacene sublimation, otherwise the molecules would not stay on the surface due to their high vapor pressure at higher temperatures. [27]

The capability to prepare the samples and perform various measurements all *in situ* in the UHV sample chamber of the LEEM instrument is a major advantage. It reduces the possibility of surface contamination between sample preparation and measurement as a result of exposure to ambient pressure. Note that given the surface sensitivity of LEEM any contamination of the sample surface interferes with the measurements.

Next, we discuss a few spectroscopy techniques available in LEEM.

2.6 LEEM-IV spectroscopy

The intensity in any region of a LEEM image depends on the energy of the incident beam used for imaging. In other words, LEEM images of the same area of the sample obtained with different beam energies look different. Recording the intensity variations of any location on the sample surface while varying the incident beam energy (i.e. changing the sample bias voltage) within a given range, yields what is called a "LEEM-IV (intensity vs. voltage) spectrum". To obtain a LEEM-IV spectrum, typically an aperture is placed on the 0^{th}-order diffraction spot in order to prevent electrons from other diffraction peaks, as well as incoherently-scattered and secondary electrons, from affecting image intensity. Such LEEM-IV spectra are a fingerprint of the electronic and crystalline structure of the area. At low electron energies, LEEM-IV spectra are mostly determined by the unoccupied electronic DOS above the vacuum level. [28–34] Simply put, if the DOS is high at a given energy, the incoming electrons can enter the sample, resulting in lower reflectivity in the LEEM-IV spectrum. Vice versa, at energies corresponding to a band gap, the electrons cannot enter the sample and the reflectivity is high. The exact value of the reflectivity, however, depends not only on the availability of unoccupied electronic states, but also on the quantum mechanical probability of both the incident and reflected vacuum electron plane waves coupling with the unoccupied sample states. The higher this probability, the lower the reflectivity. [35]

Differences in the LEEM-IV reflectivity spectra of different regions on the sample at any given electron energy create the contrast in LEEM images. For example, the intensity variations within the LEEM image in Fig. 2.3(a) are due to differences in the LEEM-IV spectra of different pentacene layer counts.

A different approach for obtaining LEEM-IV spectra is placement of an illumination aperture on a homogeneous area on the sample and recording the intensity variations of the diffraction pattern as a function of incident beam energy. Plotting the intensity variations of the 0^{th}-order diffraction peak yields the same LEEM-IV spectrum as the one obtained by following the intensity variations of the same area in bright-field images, as explained above. This approach, however, also allows for observing the energy-dependence of the intensities of other diffraction peaks.

As an example, Fig. 2.4(a) shows a bright-field image of a Au film on mica (sample purchased from Phasis). The terrace step edges on the areas in between the bigger gaps can

be seen as narrow black lines created by Fresnel interference of the electron waves reflected from adjacent sides of the step edge. This is called “phase contrast”. Fig. 2.4(b) shows a LEEM-IV spectrum obtained on the Au film in Fig. 2.4(a). Here, the negative energies indicate that the incident electrons do not have sufficient kinetic energy to reach the sample, i.e. the sample potential is too negative. This results in total reflection, i.e. the sample acts as a perfect mirror. 0 eV corresponds to electrons that reach the sample with no kinetic energy. This energy is called the mirror-mode transition (MMT) energy. Due to the energy spread of the beam, ~250 meV, some electrons have slightly lower or higher energies at MMT energy. At positive energies, electrons interact with the sample.

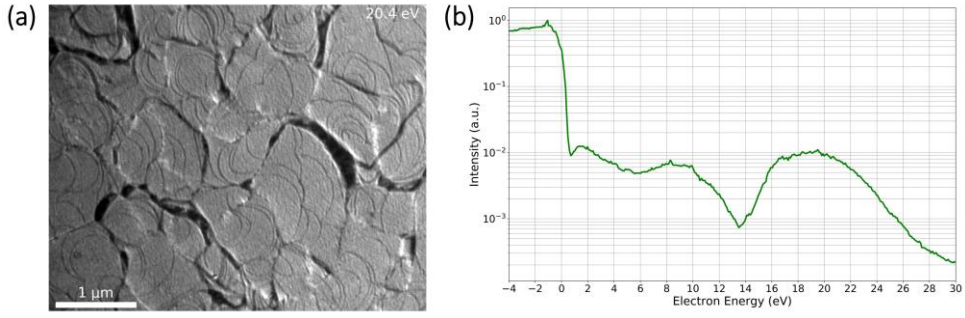

Fig. 2.4 (a) bright-field image of a Au film on mica, obtained by a beam of 20.4 eV electrons. The narrow black lines on the areas in between the bigger gaps indicate terrace step edges. They are created by Fresnel interference of the electron waves reflected from adjacent sides of the step edge. (b) LEEM-IV spectrum of Au on mica. Here, 0 eV corresponds to vacuum level. Negative energies indicate that the incident electrons do not have sufficient kinetic energy to reach the sample, resulting in total reflection. At positive energies, the incident electrons interact with the sample.

2.7 Angle-Resolved Reflected-Electron Spectroscopy (ARRES)

LEEM-IV spectra obtained as described above, follow the intensity variations of electrons with normal incidence and reflection from the sample. In other words, the incident electrons do not have any in-plane momentum when interacting with the sample. Angle-resolved reflected-electron spectroscopy (ARRES) is an extension of LEEM-IV spectroscopy as introduced above, in which the incident electrons are provided with in-plane momenta. This allows for probing the unoccupied electronic DOS across the entire Brillouin zone. ARRES is described in detail in chapter 6.

2.8 Electron Energy Loss Spectroscopy (EELS)

We discussed earlier that electrons with energies above the MMT energy reach the sample and interact with it. These electrons are either transmitted through the sample, absorbed by the sample, or reflected from it. Reflection or scattering of electrons can be either elastic or inelastic. Elastically-scattered electrons have the same kinetic energy as the incident electrons. They create a LEED pattern in the case of reflection from crystalline surfaces. On the other hand, some incident electrons lose some of their energy upon interaction with the sample, as a result of creation of excitations in the sample. Hence, they are inelastically scattered. Interaction of an incoming electron beam with the sample can also lead to creation of secondary electrons. The secondary electrons typically have low energies of only a few eV for the incident electron energies used in LEEM. These secondary electrons are accelerated by the electric field between the objective lens and the sample in the same way as photoelectrons and reflected electrons from the electron gun.

We can learn about the physical properties of the sample by analyzing the energy distribution of the electrons leaving the sample by a measurement technique called Electron Energy Loss Spectroscopy (EELS). [36–38] This is implemented in the following way. A slit is placed in the back focal plane of the objective lens ("energy slit" in Fig. 2.1). In this diffraction plane, the angular distributions of electrons with different energies occur as superimposed concentric disks of varying radii, with higher energies corresponding to bigger radii. Each disk represents the in-plane momentum distributions of the electrons with a certain energy. Fig. 2.5(a) illustrates this with three disks representative of three different electron energies. Note that only the outlines of the disks are shown. The energy slit selects a narrow slice of the diffraction space (at fixed k_x) in which the intensities from these concentric disks are superimposed. In Fig. 2.5(a), the energy slit is placed across the center of the disks ($k_x = 0$). Since the magnetic prism array is dispersive, after the beam passes through the prism, the aforementioned disks are shifted relative to each other along the dispersive direction of the magnetic prism array (x direction); see Fig. 2.5(b). As a result, the slices of the concentric disks selected by the energy slit are no longer superimposed on top of each other, but rather are shifted with respect to one another; see Fig. 2.5(b). The exact amount of the shift depends on the energy of the electrons. In the ESCHER LEEM instrument, an energy resolution of about 160 meV can be achieved for 15 keV electrons. [39] Due to the relation between the energy and the momenta of the electrons ($E \sim k^2$), the shifted slices are enveloped in a parabola, as illustrated in Fig. 2.5(c). With the energy slit placed across the center of the concentric disks, the vertex of this parabola corresponds to electrons leaving the sample with kinetic energy of 0 eV. Hence, in this manner, the energy distribution of electrons from the sample is revealed.

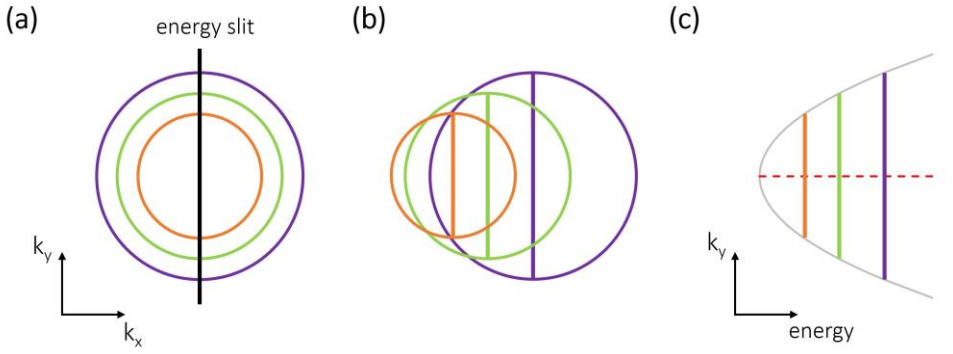

Fig. 2.5 Electron Energy Loss Spectroscopy. (a) Three superimposed concentric disks (only the outlines are shown) in the diffraction space, each containing the angular distribution of electrons from the sample with a certain energy. Higher energies correspond to larger disk radii. An energy slit selecting a slice of the diffraction space is shown. Here, the energy slit passes through the center of the disks and corresponds to k_x=0. (b) the disks are shifted relative to each other after passing through MPA1, due to the dispersive character of the prism. In other words, electrons with different energies are deflected by slightly different angles upon passing through the prism. (c) The slices of the diffraction pattern selected by the energy slit corresponding to various disks are no longer superimposed. The slices from all the possible disks form a parabola, due to the relation between the energy and the momenta of the electrons ($E \sim k^2$). The dashed red line corresponds to k_y=0. Hence, the spectrum obtained from this linecut yields the energy distribution of electrons from the sample with no in-plane momenta (k_x=k_y=0)

Fig. 2.6 shows an example of an electron energy spectrum obtained from a three-monolayer pentacene film. For this measurement, the energy slit was placed across the center of the diffraction pattern (k_x=0). The spectrum in Fig. 2.6 is a linecut passing through the vertex of the parabola along the dashed red line in Fig. 2.5(c), and hence, corresponds to electrons with no in-plane momenta ($k_x = k_y = 0$). Here, the strong peak at 10.1 eV corresponds to elastically scattered electrons, while the distribution between 0 eV and 4 eV corresponds to secondary electrons (near the vertex of the parabola). Electron energy spectra in pentacene films are further explored in chapter 5.

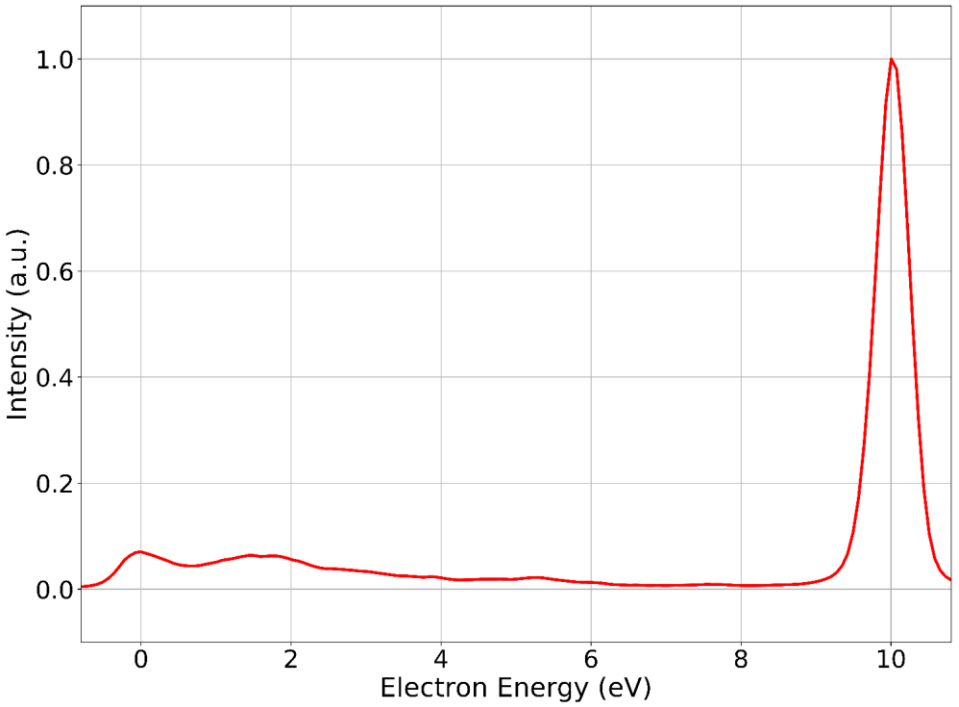

Fig. 2.6 Electron energy spectrum from a three-monolayer pentacene film. The peak at the right corresponds to elastically scattered electrons having an energy of 10.1 eV. The distribution at the left (0-4 eV) corresponds to secondary electrons.

References

[1] W. Telieps and E. Bauer, *An Analytical Reflection and Emission UHV Surface Electron Microscope*, Ultramicroscopy **17**, 57 (1985).

[2] M. P. Seah and W. A. Dench, *Quantitative Electron Spectroscopy of Surfaces: A Standard Data Base for Electron Inelastic Mean Free Paths in Solids*, Surf. Interface Anal. **1**, 2 (1979).

[3] D. Geelen, J. Jobst, E. E. Krasovskii, S. J. van der Molen, and R. M. Tromp, *Nonuniversal Transverse Electron Mean Free Path through Few-Layer Graphene*, Phys. Rev. Lett. **123**, 086802 (2019).

[4] Frank-J. Meyer zu Heringdorf, M. C. Reuter, and & R. M. Tromp, *Growth Dynamics of Pentacene Thin Films*, Nature **412**, 517 (2001).

[5] A. Al-Mahboob, J. T. Sadowski, Y. Fujikawa, K. Nakajima, and T. Sakurai, *Kinetics-Driven Anisotropic Growth of Pentacene Thin Films*, Phys. Rev. B **77**, 035426 (2008).

[6] F. J. Meyer Zu Heringdorf, M. C. Reuter, and R. M. Tromp, *The Nucleation of Pentacene Thin Films*, Appl. Phys. A **78**, 787 (2004).

[7] A. J. H. van der Torren et al., *Growing a $LaAlO_3/SrTiO_3$ Heterostructure on $Ca_2Nb_3O_{10}$ Nanosheets*, Sci. Rep. **9**, 17617 (2019).

[8] J. Kautz, M. W. Copel, M. S. Gordon, R. M. Tromp, and S. J. van der Molen, *Titration of Submonolayer Au Growth on Si(111)*, Phys. Rev. B **89**, 035416 (2014).

[9] A. J. H. van der Torren, S. J. van der Molen, and J. Aarts, *Imaging Pulsed Laser Deposition Growth of Homo-Epitaxial $SrTiO_3$ by Low-Energy Electron Microscopy*, Nanotechnology **27**, 495702 (2016).

[10] A. J. H. van der Torren, Z. Liao, C. Xu, N. Gauquelin, C. Yin, J. Aarts, and S. J. van der Molen, *Formation of a Conducting $LaAlO_3/SrTiO_3$ Interface Studied by Low-Energy Electron Reflection during Growth*, Phys. Rev. Mater. **1**, 075001 (2017).

[11] N. M. Buckanie and F. J. Meyer zu Heringdorf, *Photoemission Electron Microscopy Study of Anthracene Growth on Si(111)*, Surf. Sci. **601**, 1701 (2007).

[12] T. Yasue, T. Koshikawa, and E. Bauer, *Low Energy Electron Microscopy/Diffraction Study on Growth of Ge on Si(113) Surface*, J. Vac. Sci. Technol. B **20**, 2496 (2002).

[13] A. Pavlovska, E. Bauer, and M. Giessen, *Low Energy Electron Microscopy Study of In on Si(111)*, J. Vac. Sci. Technol. B **20**, 2478 (2002).

[14] H. W. Liu, H. T. Yuan, N. Fukui, L. Zhang, J. F. Jia, Y. Iwasa, M. W. Chen, T. Hashizume, T. Sakurai, and Q. K. Xue, *Growth of Topological Insulator Bi_2Te_3 Ultrathin Films on Si(111) Investigated by Low-Energy Electron Microscopy*, Cryst. Growth Des. **10**, 4491 (2010).

[15] H. Hibino, S. Wang, C. M. Orofeo, and H. Kageshima, *Growth and Low-Energy Electron Microscopy Characterizations of Graphene and Hexagonal Boron Nitride*, Prog. Cryst. Growth Ch. **62**, 155 (2016).

[16] C. Klein, R. Ramchal, M. Farle, and A. K. Schmid, *Direct Imaging of Spin-Reorientation Transitions in Ultrathin Ni Films by Spin-Polarized Low-Energy Electron Microscopy*, Surf. Interface Anal. **38**, 1550 (2006).

[17] A. Makoveev, P. Procházka, A. Shahsavar, L. Kormoš, T. Krajňák, V. Stará, and J. Čechal, *Kinetic Control of Self-Assembly Using a Low-Energy Electron Beam*, Appl. Surf. Sci. **600**, 154106 (2022).

[18] R. Zdyb, A. Locatelli, S. Heun, S. Cherifi, R. Belkhou, and E. Bauer, *Nanomagnetism Studies with Spin-Polarized Low-Energy Electron Microscopy and x-Ray Magnetic Circular Dichroism Photoemission Electron Microscopy*, Surf. Interface Anal. **37**, 239 (2005).

[19] K. L. Man, M. S. Altman, and H. Poppa, *Spin Polarized Low Energy Electron Microscopy Investigations of Magnetic Transitions in Fe/Cu(100)*, Surf. Sci. **480**, 163 (2001).

[20] S. M. Schramm, J. Kautz, A. Berghaus, O. Schaff, R. M. Tromp, and S. J. van der Molen, *Low-Energy Electron Microscopy and Spectroscopy with ESCHER: Status and Prospects*, IBM J. Res. & Dev. **55**, 1:1 (2011).

[21] R. M. Tromp, J. B. Hannon, A. W. Ellis, W. Wan, A. Berghaus, and O. Schaff, *A New Aberration-Corrected, Energy-Filtered LEEM/PEEM Instrument. I. Principles and Design*, Ultramicroscopy **110**, 852 (2010).

[22] R. M. Tromp, J. B. Hannon, W. Wan, A. Berghaus, and O. Schaff, *A New Aberration-Corrected, Energy-Filtered LEEM/PEEM Instrument II. Operation and Results*, Ultramicroscopy **127**, 25 (2013).

[23] R. M. Tromp, M. Mankos, M. C. Reuter, A. W. Ellis, and M. Copel, *A New Low Energy Electron Microscope*, Surf. Rev. Lett. **5**, 1189 (1998).

[24] R. H. Fowler and L. Nordheim, *Electron Emission in Intense Electric Fields*, Proc. R. Soc. Lond. A **119**, 173 (1928).

[25] K. S. Novoselov, D. Jiang, F. Schedin, T. J. Booth, V. V Khotkevich, S. V Morozov, and A. K. Geim, *Two-Dimensional Atomic Crystals*, P. Natl. Acad. Sci. **102**, 10451 (2005).

[26] K. S. Novoselov, A. K. Geim, S. V Morozov, D. Jiang, Y. Zhang, S. V Dubonos, I. V Grigorieva, and A. A. Firsov, *Electric Field Effect in Atomically Thin Carbon Films*, Science **306**, 666 (2004).

[27] V. Oja and E. M. Suuberg, *Vapor Pressures and Enthalpies of Sublimation of Polycyclic Aromatic Hydrocarbons and Their Derivatives*, J. Chem. Eng. Data **43**, 486 (1998).

[28] E. Bauer, *Surface Microscopy with Low Energy Electrons* (2014), Springer New York, ISBN: 978-1-4939-0934-6

[29] J. B. Pendry, *The Application of Pseudopotentials to Low-Energy Electron Diffraction II: Calculation of the Reflected Intensities*, J. Phys. C: Solid State Phys. **2**, 2273 (1969).

[30] J. B. Pendry, *Theory of Photoemission*, Surf. Sci. **57**, 679 (1976).

[31] J. Jobst, J. Kautz, D. Geelen, R. M. Tromp, and S. J. van der Molen, *Nanoscale Measurements of Unoccupied Band Dispersion in Few-Layer Graphene*, Nat. Commun. **6**, 8926 (2015).

[32] J. Jobst, A. J. H. van der Torren, E. E. Krasovskii, J. Balgley, C. R. Dean, R. M. Tromp, and S. J. van der Molen, *Quantifying Electronic Band Interactions in van der Waals Materials Using Angle-Resolved Reflected-Electron Spectroscopy*, Nat. Commun. **7**, 13621 (2016).

[33] V. N. Strocov, E. E. Krasovskii, W. Schattke, N. Barrett, H. Berger, D. Schrupp, and R. Claessen, *Three-Dimensional Band Structure of Layered $TiTe_2$: Photoemission Final-State Effects*, Phys. Rev. B **74**, 195125 (2006).

[34] V. N. Strocov, H. I. Starnberg, and P. O. Nilsson, *Mapping the Excited-State Bands above the Vacuum Level with VLEED: Principles, Results for Cu, and the Connection to Photoemission*, J. Phys.: Condens. Matter. **8**, 7539 (1996).

[35] J. I. Flege and E. E. Krasovskii, *Intensity-Voltage Low-Energy Electron Microscopy for Functional Materials Characterization*, Phys. Status Solidi RRL **8**, 463 (2014).

[36] Y. Fujikawa, T. Sakurai, and R. M. Tromp, *Micrometer-Scale Band Mapping of Single Silver Islands in Real and Reciprocal Space*, Phys. Rev. B **79**, 121401(R) (2009).

[37] R. M. Tromp, Y. Fujikawa, J. B. Hannon, A. W. Ellis, A. Berghaus, and O. Schaff, *A Simple Energy Filter for Low Energy Electron Microscopy/Photoelectron Emission Microscopy Instruments*, J. Phys.: Condens. Matter. **21**, 314007 (2009).

[38] Y. Fujikawa, T. Sakurai, and R. M. Tromp, *Surface Plasmon Microscopy Using an Energy-Filtered Low Energy Electron Microscope*, Phys. Rev. Lett. **100**, 126803 (2008).

[39] S. Schramm, PhD Thesis (Leiden University): *Imaging with Aberration-Corrected Low Energy Electron Microscopy* (2013), ISBN: 978-90-8593-152-2. http://hdl.handle.net/1887/20843